




Solar Kinetic Energy and Cross Helicity Spectra

Hongqi Zhang¹ and Axel Brandenburg^{2,3,4,5} 

¹ Key Laboratory of Solar Activity, National Astronomical Observatories, Chinese Academy of Sciences, Beijing 100012, People's Republic of China; h Zhang@bao.ac.cn

² Nordita, KTH Royal Institute of Technology and Stockholm University, Roslagstullsbacken 23, SE-10691 Stockholm, Sweden

³ JILA and Department of Astrophysical and Planetary Sciences, University of Colorado, Boulder, CO 80303, USA

⁴ Department of Astronomy, AlbaNova University Center, Stockholm University, SE-10691 Stockholm, Sweden

⁵ Laboratory for Atmospheric and Space Physics, University of Colorado, Boulder, CO 80303, USA

Received 2018 April 27; revised 2018 July 5; accepted 2018 July 12; published 2018 July 31

Abstract

We develop a formalism that treats the calculation of solar kinetic energy and cross helicity spectra in an equal manner to that of magnetic energy and helicity spectra. The magnetic helicity spectrum is shown to be equal to the vertical part of the current helicity spectrum divided by the square of the wavenumber. For the cross helicity, we apply the recently developed two-scale approach globally over an entire active region to account for the sign change between the two polarities. Using vector magnetograms and Dopplergrams of NOAA 11158 and 12266, we show that kinetic and magnetic energy spectra have similar slopes at intermediate wavenumbers, where the contribution from the granulation velocity has been removed. At wavenumbers around 0.3 Mm^{-1} , the magnetic helicity is found to be close to its maximal value. The cross helicity spectra are found to be within about 10% of the maximum possible value. Using the two-scale method for NOAA 12266, the global cross helicity spectrum is found to be particularly steep, similarly to what has previously been found in theoretical models of spot generation. In the quiet Sun, by comparison, the cross helicity spectrum is found to be small.

Key words: dynamo – Sun: activity – Sun: magnetic fields – Sun: photosphere

1. Introduction

The photospheric plasma is thought to be in a state of fully developed magnetohydrodynamic turbulence at high magnetic Reynolds numbers. The spectral slope of the turbulent velocity field is believed to be of the order of $-5/3$, as theoretically proposed by Kolmogorov (1941) and Obukhov (1941), and as is also expected from the theory of nonhelical hydromagnetic turbulence when the magnetic field is moderately strong and therefore noticeably anisotropic (Goldreich & Sridhar 1995). For decaying turbulence, on the other hand, Lee et al. (2010) found that the scaling depends on the field strength, and a shallower Iroshnikov–Kraichnan $k^{-3/2}$ spectrum (Iroshnikov 1963; Kraichnan 1965) occurs for weaker fields and a steeper k^{-2} weak-turbulence spectrum for stronger fields (Galtier et al. 2000; Brandenburg et al. 2015); see the reviews by Brandenburg & Subramanian (2005) and Brandenburg & Nordlund (2011) for a discussion of the respective phenomenologies in the three cases. The observations of magnetic and velocity fields in the solar atmosphere provide a window to analyze solar hydromagnetic turbulence through their power spectra and compare with earlier work (Abramenko 2005; Abramenko & Yurchyshyn 2010b; Stenflo 2012; Zhao & Chou 2013).

The technique used to obtain the scale dependence of magnetic helicity through observations is reminiscent of that of Matthaeus et al. (1982), who made the assumption of isotropy to express the Fourier transform of the two-point correlation tensor of the magnetic field in terms of the Fourier transforms of the magnetic field. Their approach made use of one-dimensional spectra obtained from time series of all three magnetic field components and was applied to in situ measurements in the solar wind. The Taylor hypothesis (Taylor 1938) was used to relate the two-point correlation function in time to one in space. In the work of Zhang et al.

(2014, 2016), again the assumption of isotropy was made, but a full two-dimensional array of magnetic field vectors was used, so the Taylor hypothesis was not invoked. They applied this technique to a number of active regions to determine magnetic energy and helicity spectra and their change with time. The current helicity spectrum was estimated from the magnetic helicity spectrum under the assumption of isotropy, and its modulus showed a $k^{-5/3}$ spectrum at intermediate wavenumbers. A similar power law is also obtained for the magnetic energy spectrum. These are largely consistent with expectations from the turbulence simulations discussed by Brandenburg & Subramanian (2005).

In this letter, we compare power spectra of the magnetic field with those of the velocity field inferred from photospheric vector magnetograms and Dopplergrams in solar active regions NOAA 11158, 12266, and the quiet Sun. In addition to the kinetic energy spectrum, we also compute cross helicity spectra. Cross helicity has been determined previously using both theory (Pipin et al. 2011; Rüdiger et al. 2011; Brandenburg and Rädler 2013; Yokoi 2013) and observations (Kuzanyan et al. 2007; Rüdiger et al. 2012; Zhao et al. 2014), and it may play a direct role in the production of active regions (Brandenburg et al. 2014). However, cross helicity spectra have previously only been obtained from theory.

2. Basic Formalism

We begin by reviewing briefly the method of Zhang et al. (2014). They introduced the two-point correlation tensor of the magnetic field, $\langle B_i(\mathbf{x}, t) B_j(\mathbf{x} + \boldsymbol{\xi}, t) \rangle$, and write its Fourier transform with respect to $\boldsymbol{\xi}$ as

$$\langle \tilde{B}_i(\mathbf{k}, t) \tilde{B}_j^*(\mathbf{k}', t) \rangle = \Gamma_{ij}(\mathbf{k}, t) \delta^2(\mathbf{k} - \mathbf{k}'), \quad (1)$$

where the tildes indicate Fourier transformation, i.e., $\tilde{B}_i(\mathbf{k}, t) = \int B_i(\mathbf{x}, t) e^{i\mathbf{k}\cdot\mathbf{x}} d^2\xi$, and the asterisk denotes complex

conjugation. Under the assumption of isotropy, the spectral correlation tensor $\Gamma_{ij}(\mathbf{k}, t)$ can be written as

$$\Gamma_{ij}(\mathbf{k}, t) = \frac{2E_M(k, t)}{4\pi k} (\delta_{ij} - \hat{k}_i \hat{k}_j) + \frac{iH_M(k, t)}{4\pi k} \varepsilon_{ijk} k_k, \quad (2)$$

where $E_M(k, t)$ and $H_M(k, t)$ are the shell-integrated magnetic energy and helicity spectra, respectively, $\hat{\mathbf{k}} = \mathbf{k}/k$ is the unit vector of \mathbf{k} , and $k = (k_x^2 + k_y^2)^{1/2}$ is the wavenumber. The spectra are normalized such that $\int E_M dk = \langle B^2 \rangle / 2$ and $\int H_M dk = \langle \mathbf{A} \cdot \mathbf{B} \rangle$, where \mathbf{A} is the magnetic vector potential with $\mathbf{B} = \nabla \times \mathbf{A}$. The two spectra can also be computed as (cf. Brandenburg & Nordlund 2011)

$$E_M(k) = \frac{1}{2} \sum_{k_- < |\mathbf{k}| \leq k_+} |\tilde{\mathbf{B}}(\mathbf{k})|^2, \quad (3)$$

$$H_M(k) = \frac{1}{2} \sum_{k_- < |\mathbf{k}| \leq k_+} (\tilde{\mathbf{A}} \cdot \tilde{\mathbf{B}}^* + \tilde{\mathbf{A}}^* \cdot \tilde{\mathbf{B}}), \quad (4)$$

where $k_{\pm} = k \pm \delta k / 2$ and $\delta k = 2\pi/L$ is the wavenumber increment and also the smallest wavenumber in the plane L^2 with L being the size of the magnetograms. Following common convention, the magnetic energy density is measured in G^2 , so the units of the spectrum $E_M(k)$ are $G^2 \text{ cm}$ (Abramenko & Yurchyshyn 2010a). To compute the magnetic helicity spectrum, Zhang et al. (2014) used the expression

$$kH_M(k, t) = 4\pi k \text{Im} \langle \cos \phi_k \Gamma_{yz} - \sin \phi_k \Gamma_{xz} \rangle_{\phi_k}, \quad (5)$$

where we have defined the polar angle in wavenumber space so that $k_x = k \cos \phi_k$ and $k_y = k \sin \phi_k$. The angle brackets with subscript ϕ_k denote averaging over annuli in wavenumber space. Note that only the xz and yz components enter, so Equation (5) becomes

$$kH_M(k, t) = 4\pi k \text{Im} \langle (k_x \tilde{B}_y - k_y \tilde{B}_x) \tilde{B}_{\parallel}^* \rangle_{\phi_k}. \quad (6)$$

Thus, by introducing

$$\tilde{A}_{\parallel} = (-ik_x \tilde{B}_y + ik_y \tilde{B}_x) / k^2 \equiv \tilde{J}_{\parallel} / k^2, \quad (7)$$

with \tilde{J}_{\parallel} being the Fourier transform of $J_{\parallel} \equiv \partial_x B_y - \partial_y B_x$, we can relate $H_M(k, t)$ to the vertical part indicated by (\parallel) of the current helicity spectrum, $H_C(k, t) = k^2 H_M(k, t)$, which was already used in Zhang et al. (2014). Therefore, instead of working with Equation (4), we compute from now on

$$E_M(k) = \frac{1}{2} \sum_{k_- < |\mathbf{k}| \leq k_+} |\tilde{\mathbf{B}}_{\parallel}(\mathbf{k})|^2, \quad (8)$$

$$H_M(k) = \frac{1}{2} \sum_{k_- < |\mathbf{k}| \leq k_+} (\tilde{A}_{\parallel} \tilde{B}_{\parallel}^* + \tilde{A}_{\parallel}^* \tilde{B}_{\parallel}), \quad (9)$$

which is equivalent to Equations (3) and (4). Note that $E_M(k)$ and $H_M(k)$ satisfy the realizability condition $2E_M \geq |H_M|$, which is also the reason why we always plot the scaled combinations $2E_M(k)$ and $kH_M(k)$. This allows us to judge how close to fully helical the magnetic field is at each wavenumber.

An analysis similar to that of the magnetic field can also be done for the velocity. Only the Doppler velocity field can readily be observed. Thus, we compute vertical kinetic energy

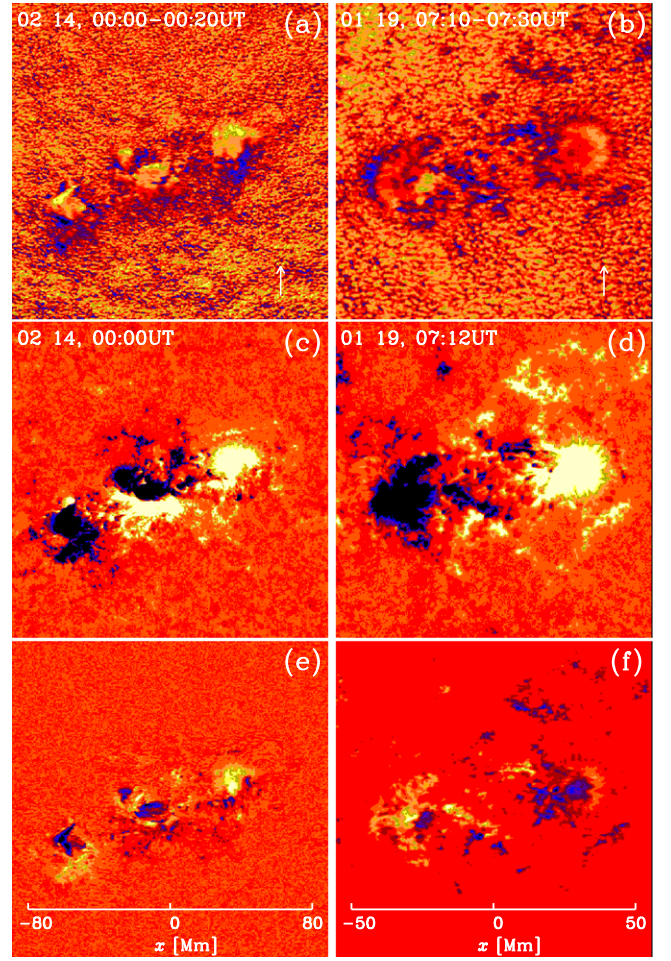


Figure 1. Doppler velocity field v_{\parallel} (top), longitudinal magnetic field B_{\parallel} (middle), and their product $v_{\parallel} B_{\parallel}$ (bottom), for active regions NOAA 11158 (left, field of view $256'' \times 256''$) on 2011 February 14 and NOAA 12266 (right, field of view $150'' \times 150''$) on 2015 January 19. Yellow (blue) shades show positive (negative), corresponding to the upward (downward) directions.

and cross helicity spectra as

$$E_K(k) = \frac{1}{2} \sum_{k_- < |\mathbf{k}| \leq k_+} |\tilde{v}_{\parallel}(\mathbf{k})|^2, \quad (10)$$

$$H_X(k) = \frac{1}{2} \sum_{k_- < |\mathbf{k}| \leq k_+} (\tilde{v}_{\parallel} \tilde{B}_{\parallel}^* + \tilde{v}_{\parallel}^* \tilde{B}_{\parallel}). \quad (11)$$

Defining $q \equiv \sqrt{4\pi\rho_0}$, the realizability condition reads

$$qE_K(k) + E_M(k)/q \geq |H_X(k)|, \quad (12)$$

where we assume $\rho_0 = 10^{-6} \text{ g cm}^{-3}$ for the density and ignore density fluctuations. As v_{\parallel} is measured in m s^{-1} and B_{\parallel} in G, we have $q = 100 \text{ cm m}^{-1} \sqrt{4\pi\rho_0}$. We determine $E_K(k)$ and $H_X(k)$ to study the spectral distribution of the line-of-sight velocity, and its relationship with that of the magnetic field.

For the cross helicity, there is a particular problem when considering bipolar active regions. We expect the cross helicity to be proportional to the mean ambient magnetic field (Rüdiger et al. 2011). It will therefore have contributions of opposite signs from the two poles of a bipolar region, leading to cancelation; see Figure 1 for visualizations of v_{\parallel} , B_{\parallel} , and $v_{\parallel} B_{\parallel}$ for the active regions NOAA 11158 and 12266.

NOAA 12266 has two clearly separated poles. A suitable technique to obtain a spectrum encompassing the entire bipolar

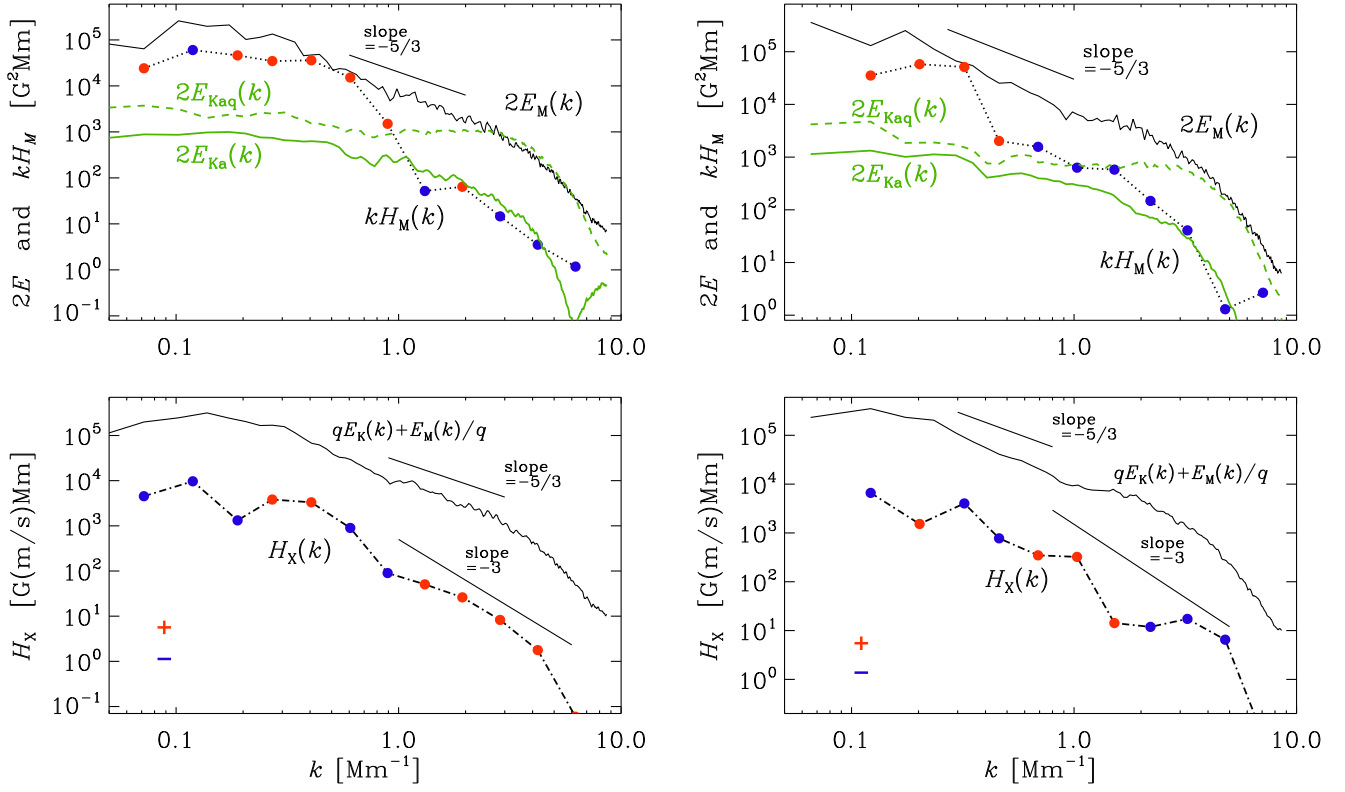


Figure 2. The upper panels show spectra of magnetic energy $E_M(k)$ (black solid lines), normalized magnetic helicity $kH_M(k)$ (black dotted lines; red and blue symbols denote positive and negative values, respectively) and kinetic energy $E_{Kaq}(k)$ (green dashed lines for kinetic energy of the quiet Sun) and $E_{Ka}(k)$ (green solid lines for kinetic energy related to magnetic features only) in active region NOAA 11158 (left) and NOAA 12266 (right). The lower panels show $qE_K(k) + E_M(k)/q$ (solid lines) and $H_X(k)$ (dashed-dotted lines; red and blue symbols denote positive and negative values, respectively).

region is the two-scale approach of Brandenburg et al. (2017), who applied it to measuring magnetic helicity for the entire solar disk, taking the systematic sign change across the equator into account; see also Singh et al. (2018). This technique allows us to incorporate the sign change as a sinusoidal modulation proportional to $\sin \mathbf{K} \cdot \mathbf{x}$ with wavevector \mathbf{K} and, in principle, arbitrary phase shifts, which are not considered here. Equation (11) then becomes

$$H_X(\mathbf{K}, k) = \sum_{k_- < |\mathbf{k}| \leq k_+} \tilde{v}_{\parallel}(\mathbf{k} + \mathbf{K}/2) \tilde{B}_{\parallel}^*(\mathbf{k} - \mathbf{K}/2), \quad (13)$$

which is complex, and its real part agrees with Equation (11) for $\mathbf{K} = 0$. For a bipolar region aligned in the x direction with an approximate separation d , we have $\mathbf{K} = (\pi/d, 0)$. Analogous to Brandenburg et al. (2017), the relevant spectrum is then $-\text{Im} H_X(\mathbf{K}, k)$. We return to this below when discussing concrete examples.

3. Comparison of the Spectra

Figure 1 shows the Doppler velocity and the corresponding longitudinal component of the vector magnetic field in the active regions NOAA 11158 on 2011 February 14 and NOAA 12266 on 2015 January 19 by the Helioseismic and Magnetic Imager (HMI) on board the *Solar Dynamics Observatory* (SDO). To obtain a representative nearly stationary pattern, we averaged over a continuous series of Dopplergrams observed during 20 minutes. The contribution from the five-minute oscillation is thus basically removed. However, projection effects have not been compensated for. A prominent Evershed flow can be seen in the strong magnetic

structures of NOAA 11158 (S20W17) due to its location southwest of disk center. We can see a pattern of small-scale velocity nearby the active region. A similar situation can also be found in the active region NOAA 12266 (S06E06) located near disk center. These small-scale velocity patterns are indicated by arrows in Figure 1. Thus, the flow fields in Figure 1 are expected have contributions both from the active regions and the quiet Sun in its proximity.

Figure 2 shows magnetic energy and scaled helicity spectra, $E_M(k)$ and $kH_M(k)$, respectively, inferred from the photospheric vector magnetograms of NOAA 11158 (cf. Zhang et al. 2014) and 12266, along with the corresponding kinetic energy spectra inferred from the Dopplergrams of Figure 1. To reduce fluctuations in the helicity spectra, we have averaged their values within logarithmically spaced wavenumber intervals. In the range of wavenumbers $k = 0.5\text{--}2.5 \text{ Mm}^{-1}$, the mean slopes of $E_M(k)$ and $k|H_M(k)|$ are -1.8 and -3.4 , respectively, for active region NOAA 11158, and -1.5 and -2.1 , respectively, for active region NOAA 12266. The temporal variation of the slopes of $E_M(k)$ and $k|H_M(k)|$ of active regions was discussed by Zhang et al. (2016). The green dashed lines $E_{Kaq}(k)$ show kinetic energy spectra of the two active regions and also those of the quiet Sun. A similar result was shown by Zhao & Chou (2013) with the continuous high spatial resolution Doppler observations of the Sun by SDO/HMI. They determined the power from the convective flows in the $k\omega$ diagram and found that the location of the convective peak is shifted toward lower wavenumbers in the power spectrum obtained from the sunspot compared to that of the quiet Sun.

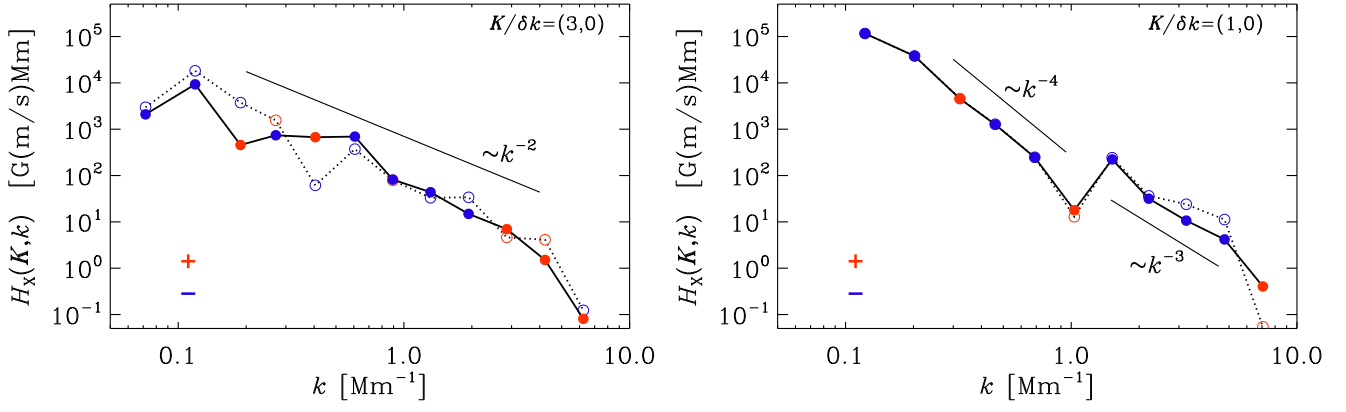


Figure 3. Cross helicity $H_X(\mathbf{K}, k)$ with two-scale analysis for active regions NOAA 11158 (left) and NOAA 12266 (right) using $\mathbf{K}/\delta k = (3, 0)$ and $(1, 0)$, respectively; see Equation (13). Red and blue symbols denote positive and negative values, respectively. Dotted lines with open symbols refer to strong fields only (the line-of-sight magnetic field exceeds ± 50 G), while solid lines with closed symbols apply to all points. \mathbf{K} is given in units of $\delta k = 2\pi/L$ defined below Equation (4).

The green solid lines $E_{K_a}(k)$ in Figure 2 show kinetic energy spectra of the active region relative to the magnetic structures with $|B_{\parallel}| > 50$ G only. (The subscript “a” refers to active region.) We find that the uprise of kinetic energy near $k = 2\text{--}5 \text{ Mm}^{-1}$ is now removed for both active regions, and the slopes of the spectra of kinetic energy are consistent with a $k^{-3/3}$ spectrum. This removal is done by setting the velocity to zero at those points where $|B_{\parallel}| < 50$ G just prior to taking the Fourier transform. In the range of wavenumbers $k = 0.5\text{--}2.5 \text{ Mm}^{-1}$, the mean slopes of E_{K_a} are -1.4 for NOAA 11158 and -1.5 for NOAA 12266. They are similar to those of magnetic energy $E_M(k)$ and scaled magnetic helicity $kH_M(k)$ in the photosphere in the range $k = 1\text{--}2 \text{ Mm}^{-1}$. While for NOAA 11158 the slope of $E_{K_{aq}}$ is 0.05, for NOAA 12266 it is -0.2 in the range $k = 0.5\text{--}2.5 \text{ Mm}^{-1}$. (The subscript “aq” refers to the combination of active region and quiet Sun.) The kinetic energy spectra $E_{K_{aq}}(k)$ in the range $k = 2\text{--}5 \text{ Mm}^{-1}$ reflect the typical scale of the quiet Sun, which has contributions from the granulation.

The $H_X(k)$ spectra of Equation (11) have similar slopes as $qE_K + E_M/q$ with $|H_X|$ being about 10 times smaller than the limit given by the total energy; see Equation (12). However, it has no definite sign. This is different when taking the cancellation from the bipolarity into account. The two-scale method correlates functions whose wavenumbers differ by a small amount. Consider as an example $v_{\parallel} = \sin k_+ x$ and $B_{\parallel} = \cos k_- x$ with $k_{\pm} = k \pm \delta k$ and $\delta k = \pi/d = 2\pi/L$ being the lowest wavenumber of the domain, then

$$2v_{\parallel}B_{\parallel} = \sin Kx + \sin 2kx, \quad (14)$$

with K being the x component of \mathbf{K} , has a low-wavenumber modulation proportional to $\sin Kx$ with sign changes between the bipoles separated by d . Comparing with Figure 1(f) for NOAA 12266, where $d \approx 50 \text{ Mm}$, the sign of $v_{\parallel}B_{\parallel}$ changes from positive values for $x < 0$ to negative ones for $x > 0$. This is then the other way around what is implied by the example given in Equation (14). Therefore, we expect $-\text{Im } H_X(\mathbf{K}, k)$ itself to be negative. This is indeed the case; see Figure 3, which shows that $-\text{Im } H_X(\mathbf{K}, k)$ is mostly negative for NOAA 12266.

For NOAA 11158, there are two pairs of bipoles interlaced. Each pair has an approximate separation $d \approx L/3$, but the interlacing is not ideal and partially overlapping. We tried

$K_x/\delta k = 1\text{--}3$, but none had as clean a spectrum as NOAA 12266. In Figure 1, we show for NOAA 11158 the spectrum for $K_x/\delta k = 3$, which had the least sign changes and is mostly negative—in broad agreement with a $\sin 3\delta k x$ modulation in Figure 1(e). For NOAA 12266, on the other hand, $K_x/\delta k = 1$ was found to give the least sign changes—in agreement with a $\sin \delta k x$ modulation in Figure 1(f).

A negative correlation between a large-scale field proportional to $B_0 \sin Kx$ and a correlation of the form $\langle v_{\parallel}B_{\parallel} \rangle \approx -(\eta_T/H_{\rho}) \sin Kx$ is theoretically expected (Rüdiger et al. 2011), where η_T is the turbulent magnetic diffusivity and H_{ρ} is the density scale height. Using $\langle v_{\parallel}B_{\parallel} \rangle = \int H_X(\mathbf{K}, k) dk \approx -11,000 \text{ G m s}^{-1}$ and $B_0 \approx B_{\text{rms}} \approx 300 \text{ G}$, we have $\langle v_{\parallel}B_{\parallel} \rangle/B_0 \approx 40 \text{ m s}^{-1}$ and $H_{\rho} = 1 \text{ Mm}$ yields $\eta_T \approx 4 \times 10^{11} \text{ cm}^2 \text{ s}^{-1}$, which is about 10 times less than what was found by Rüdiger et al. (2012).

The slope for NOAA 12266 is between -3 and -4 , which is much steeper than that for NOAA 11158, where the slope was -2 . A steeper slope, especially at small k , is of interest when interpreting the $H_X(\mathbf{K}, k)$ spectrum as an indicator for inverse cascading being a possible mechanism for forming magnetic flux concentrations (Brandenburg et al. 2014). However, there are sign changes at $k \approx 0.3$ and 1 Mm^{-1} , which may not be compatible with this interpretation. On the other hand, a jump similar to that at $k \approx 1 \text{ Mm}^{-1}$ has also been seen in the simulations; see Figure 19 of Brandenburg et al. (2014).

For comparison with the velocity field of active regions, we show in Figure 4 the kinetic energy spectra for the velocity field of the quiet Sun near the center of the solar disk. $E_{K_{mq}}$ shows the spectrum of the whole velocity field in the field of view of the quiet Sun, and it is almost consistent with the results of Zhao & Chou (2013), while E_{K_m} shows that of the velocity field for magnetic fields with $|B_{\parallel}| > 50$ G only. (Here the subscript “mq” refers to the whole region in the field of view in the quiet Sun.) Due to the averaging over a series of continuous Dopplergrams observed during 20 minutes, the contribution from the five-minute oscillation has effectively been removed in our analyzed velocity field. $E_M(k)$ shows the spectrum of the magnetic energy inferred from the longitudinal component of the magnetic field. In the range of wavenumbers $k = 0.5\text{--}2.5 \text{ Mm}^{-1}$, the mean slope of magnetic energy E_M is -1.0 and that of E_{K_m} is 0.2. (Here the subscript “m” refers to the kinetic energy relative to areas with magnetic field only.) These are shallower than the $k^{-5/3}$ Kolmogorov spectrum.

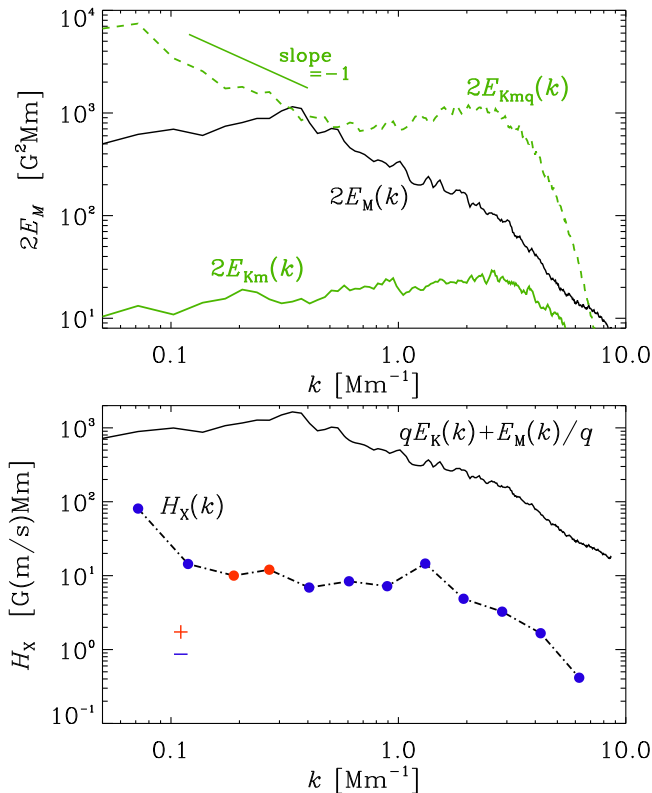


Figure 4. The upper panel shows spectra of magnetic energy $E_M(k)$ (black solid lines), kinetic energy $E_{Kmq}(k)$ (green dashed lines, for the whole velocity in the field of view of the quiet Sun) and $E_{Km}(k)$ (green solid lines for the velocity related with magnetic features only). The lower panel shows $qE_K(k) + E_M(k)/q$ (solid lines) and $H_x(k)$ (dashed-dotted lines; red and blue symbols denote positive and negative values, respectively).

4. Conclusions

Our combined analysis of velocity and magnetic fields has shown that, within active regions, kinetic and magnetic energy spectra have similar slopes at intermediate scales. Here the field is also close to maximally helical. The magnetic helicity spectra of Zhang et al. (2014, 2016) are found to be identical to those composed of just A_{\parallel} and B_{\parallel} . This is analogous to the similarly constructed current helicity, $\langle J_{\parallel} B_{\parallel} \rangle$, which is frequently employed in solar physics. The helicity spectra are gauge-independent owing to the assumed horizontal periodicity and independence of z . This assumption affects only the smallest wavenumbers. Unlike $\langle J_{\parallel} B_{\parallel} \rangle$, which captures helicity effects only on small scales or high wavenumbers, here we have access to the helicity decomposition into different wavenumbers.

Quite analogously, we have constructed cross helicity spectra. Their signs switch with the sign of the mean vertical magnetic field, which is the reason we have adopted here the two-scale approach. This approach is familiar from mean-field dynamo theory (Roberts & Soward 1975) and has recently been applied to solar magnetic helicity spectra (Brandenburg et al. 2017; Singh et al. 2018), but it is the first time that it has been applied to cross helicity. It allows us to capture properties of global spectra, avoiding cancellation from the different

polarities of bipolar regions. This approach worked particularly well for NOAA 12266, where the separation of the two polarities is about half the extent of the magnetogram. By contrast, in NOAA 11158, two pairs of polarities are interlaced, making the direct application of the two-scale approach less straightforward. For NOAA12266, the spectral slope of the cross helicity is found to be -4 . A steep slope is suggestive of an inverse cascade phenomenon of cross helicity (Brandenburg et al. 2014) and can be a possible mechanism responsible for causing magnetic flux concentrations into spots. Further work incorporating a larger sample of active regions and a global analysis would be an important future extension of this work.

This study is supported by grants from the National Natural Science Foundation (NNSF) of China under the project grants 11673033, 11427803, 11427901 and Huairou Solar Observing Station of National Astronomical Observatories, Chinese Academy of Sciences. This work has been supported in part by the NSF Astronomy and Astrophysics Grants Program (grant 1615100), and the University of Colorado through its support of the George Ellery Hale visiting faculty appointment.

ORCID iDs

Axel Brandenburg  <https://orcid.org/0000-0002-7304-021X>

References

- Abramenko, V., & Yurchyshyn, V. 2010a, *ApJ*, 720, 717
 Abramenko, V., & Yurchyshyn, V. 2010b, *ApJ*, 722, 122
 Abramenko, V. I. 2005, *ApJ*, 629, 1141
 Brandenburg, A., Gressel, O., Jabbari, S., Kleorin, N., & Rogachevskii, I. 2014, *A&A*, 562, A53
 Brandenburg, A., Kahniashvili, T., & Tevzadze, A. G. 2015, *PRL*, 114, 075001
 Brandenburg, A., & Nordlund, Å. 2011, *RPPH*, 74, 046901
 Brandenburg, A., Petrie, G. J. D., & Singh, N. K. 2017, *ApJ*, 836, 21
 Brandenburg, A., & Rädler, K.-H. 2013, *GApFD*, 107, 207
 Brandenburg, A., & Subramanian, K. 2005, *A&A*, 439, 835
 Galtier, S., Nazarenko, S. V., Newell, A. C., & Pouquet, A. 2000, *JPIPh*, 63, 447
 Goldreich, P., & Sridhar, S. 1995, *ApJ*, 438, 763
 Iroshnikov, R. S. 1963, *AZh*, 40, 742, English translation; *Sov. Astron.*, 1964, 7, 566
 Kolmogorov, A. N. 1941, *CR Acad. Sci. USSR*, 30, 299
 Kraichnan, R. H. 1965, *PhFl*, 8, 1385
 Kuzanyan, K. M., Pipin, V. V., & Zhang, H. 2007, *AdSpR*, 39, 1694
 Lee, E., Brachet, M. E., Pouquet, A., Mininni, P. D., & Rosenberg, D. 2010, *PhRvE*, 81, 016318
 Matthaeus, W. H., Goldstein, M. L., & Smith, C. 1982, *PhRvL*, 48, 1256
 Obukhov, A. M. H. 1941, *DoSSR*, 32, 22
 Pipin, V. V., Kuzanyan, K. M., Zhang, H., & Kosovichev, A. G. 2011, *ApJ*, 743, 160
 Roberts, P. H., & Soward, A. M. 1975, *AN*, 296, 49
 Rüdiger, G., Kitchatinov, L. L., & Brandenburg, A. 2011, *SoPh*, 269, 3
 Rüdiger, G., Küker, M., & Schnerr, R. S. 2012, *A&A*, 546, A23
 Singh, N. K., Käpylä, M. J., Brandenburg, A., et al. 2018, *ApJ*, in press (arXiv:1804.04994)
 Stenflo, J. O. 2012, *A&A*, 541, A17
 Taylor, G. I. 1938, *RSPSA*, 164, 476
 Yokoi, N. 2013, *GApFD*, 107, 114
 Zhang, H., Brandenburg, A., & Sokoloff, D. D. 2014, *ApJL*, 784, L45
 Zhang, H., Brandenburg, A., & Sokoloff, D. D. 2016, *ApJ*, 819, 146
 Zhao, J., & Chou, D.-Y. 2013, *SoPh*, 287, 149
 Zhao, M., Wang, X., & Zhang, H. 2014, *SCPMA*, 57, 589